Check for updates

ADVANCED FUNCTIONAL MATERIALS
www.afm-journal.de

Broad-Wavelength Light-Driven High-Speed Hybrid Crystal Actuators Actuated Inside Tissue-Like Phantoms

Dong Wook Kim, Yuki Hagiwara, Shodai Hasebe, Nihal Olcay Dogan, Mingchao Zhang, Toru Asahi, Hideko Koshima, and Metin Sitti**

Research on molecular crystals exhibiting light-driven actuation has made remarkable progress through the development of various molecules and the identification of driving mechanisms. However, crystals developed to date have been driven mainly by ultraviolet (UV) or blue light irradiation, and driving by red or near-infrared (NIR) light has not been attempted yet. Herein, a broad-wavelength light-driven molecular crystals that exhibit high-speed bending by photothermal effect is developed. Titanium carbide ($Ti_3C_2T_x$) MXene nanosheets are integrated into salicylideneaniline crystals to extend the wavelength range that causes photothermally driven bending to UV, visible, and NIR light. In addition, unlike the thin pristine molecular crystals that show slow photoisomerization-induced bending only under UV light, the MXene layer enables the molecular crystals to be actuated rapidly regardless of their thickness over a wide range of wavelengths. The hybridization of molecular crystals with MXene, which exhibits strong biocompatibility as well as NIR light-driven photothermal effect, allows for the bending of the hybrid crystals inside agar phantoms mimicking biological tissue. Last, it is confirmed that MXene hybridization can be extended to common molecular crystals including various salicylideneaniline and anisole derivatives.

1. Introduction

Mechanically responsive materials that exhibit dynamic motion through external stimuli (e.g., electricity, light, heat, or chemicals) have received considerable attention in terms of basic principle studies[1,2] as well as the applications in sensors,[3] switches,[4] actuators,[5,6] and soft robotics.[7,8] Among various external stimuli, light is an ideal driving source that can transmit energy remotely and be promptly converted into mechanical energy.[5–10] As one of the mechanically responsive materials, organic molecular crystals have been spotlighted as promising light-fuelled mechanical actuators.[11–20] Compared to other photomechanical actuators made of hydrogels,[6,7] liquid crystal elastomers (LCEs),[9] or polymeric materials,[10] organic molecular crystals have advantages of facile fabrication, simple structure, fast motion, and high Young's modulus.[11,12] Various photomechanical molecular crystals of salicylideneaniline,[13–17] furylfulgide,[18] anthracene,[19] azobenzene,[20] diarylethene,[21] and benzobarrelene[22] have been developed and exhibited macroscopic motions, such as bending,[13–20] jumping,[23] and twisting,[24] and the working mechanisms, such as photoisomerization,[13,14,17,18,20–22] photodimerization,[19] and phase transition[25] have been elucidated.

Recently, we reported photothermally driven rapid bending of several salicylideneaniline crystals.[13–16] Salicylideneaniline derivatives are typical photochromic compounds that has been utilized for enol-keto photoisomerization-driven bending.[13–17] We revealed that the salicylideneaniline crystals can be bent by a non-steady temperature gradient (ΔT) in thickness direction of the crystal when the heat is generated by photoexcitation of the crystal molecules.[13–16] We also found that photothermal effect is the major driving force that induces the bending of

D. W. Kim, N. O. Dogan, M. Zhang, M. Sitti
Physical Intelligence Department
Max Planck Institute for Intelligent Systems
70569 Stuttgart, Germany
E-mail: sitti@is.mpg.de

Y. Hagiwara, S. Hasebe, T. Asahi
Graduate School of Advanced Science and Engineering
Waseda University
3-4-1 Okubo, Shinjuku-ku, Tokyo 169-8555, Japan

N. O. Dogan, M. Sitti
Institute for Biomedical Engineering
ETH Zurich 8092, Zurich, Switzerland

T. Asahi, H. Koshima
Research Organization for Nano and Life Innovation
Waseda University
513 Wasedatsurumaki-cho, Shinjuku-ku, Tokyo 162-0041, Japan
E-mail: h.koshima@kurenai.waseda.jp

M. Sitti
School of Medicine and College of Engineering
Koç University
Istanbul 34450, Turkey

The ORCID identification number(s) for the author(s) of this article can be found under https://doi.org/10.1002/adfm.202305916

© 2023 The Authors. Advanced Functional Materials published by Wiley-VCH GmbH. This is an open access article under the terms of the Creative Commons Attribution License, which permits use, distribution and reproduction in any medium, provided the original work is properly cited.

DOI: 10.1002/adfm.202305916

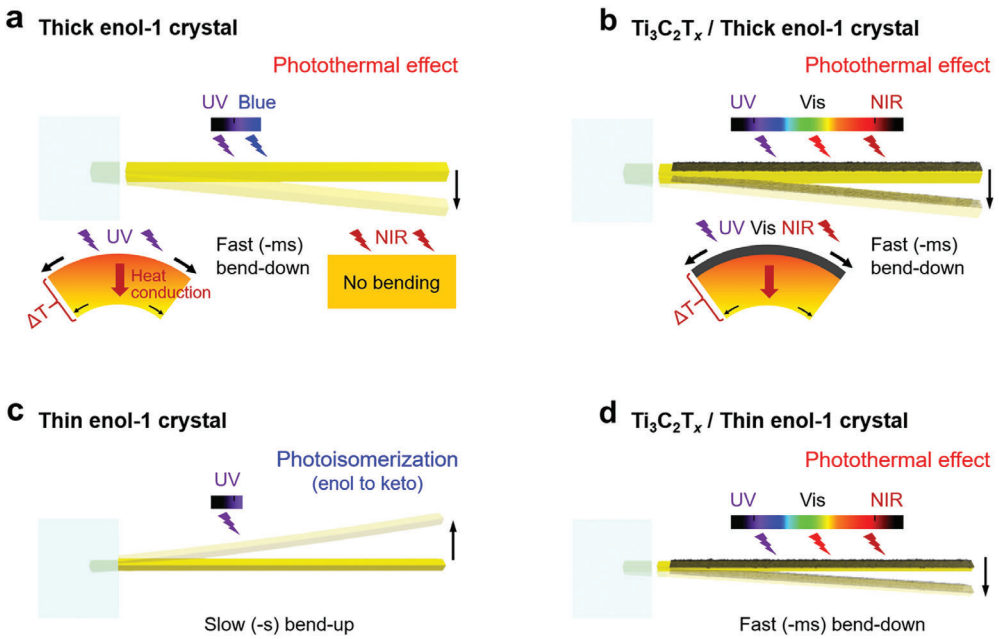


Figure 1. Photomechanical bending of enol-**1** and $Ti_3C_2T_x$-coated enol-**1** crystal cantilever beam upon light irradiation. a) Fast bend-down motion of the thick enol-**1** crystal beam upon irradiation with UV and blue light. The irradiated UV or blue light increases the temperature on the top crystal surface by photothermal effect and the temperature gradient (ΔT) formed in the crystals induces bend-down motion. b) Fast bend-down motion of the $Ti_3C_2T_x$-coated thick enol-**1** crystal beam upon irradiation with UV, visible (blue and red), and NIR light. The coated $Ti_3C_2T_x$ layer induces photothermally driven bending under broad-wavelength of light. c) Slow bend-up motion of the thin enol-**1** crystal beam upon irradiation with UV light. The UV light induces photoisomerization on the thin enol-**1** crystal molecules generating slow bend-up motion. d) Fast bend-down motion of the $Ti_3C_2T_x$-coated thin enol-**1** crystal beam by photothermal effect upon irradiation with UV, visible (blue and red), and NIR light.

relatively thick salicylideneaniline crystals, but photoisomerization is more dominant in the actuation of thin crystals.[13–16] Compared to photochemical reactions (i.e., photoisomerization or photodimerization), photothermal effect has several advantages in crystal actuation, including high speed, broad optical wavelength selectivity, and actuation of thicker crystals, and it is expected to broaden the application range of organic molecular crystals as a next-generation photo-responsive actuator. Despite these numerous studies on various photomechanical molecular crystals with different mechanisms to date, their actuation has relied mostly on ultraviolet (UV) or blue light,[11–24] but not on red or near-infrared (NIR) light. The molecular crystals that perform mechanical motion over a wide range of wavelengths from UV to visible and NIR are expected to expand the application range of photomechanical crystals to other biomedical fields such as implantable devices,[26,27] mobile microrobots,[28–30] and bioinspired engineering.[31] To develop such broad-wavelength light-driven molecular crystals, new strategies and perspectives that deviate from conventional molecular designs are required.

Here, we report organic molecular crystals (salicylideneaniline or anisole derivatives) that exhibit high-speed photothermally driven bending by a broad wavelength of light, including UV, visible, and NIR light. This is the first study of organic molecular crystals that can be driven photomechanically over a wide range of wavelengths (Table S1, Supporting Information). For the broad-wavelength light-driven crystal bending, 2D titanium carbide ($Ti_3C_2T_x$) MXene is introduced to molecular crystals. Specifically, unlike the relatively thick (>100 µm) salicylideneaniline (enol-**1**) crystal that can only be bent photothermally by UV and blue light, the $Ti_3C_2T_x$ layer coated on the thick crystal extends the photothermal crystal actuation range to red and NIR light (**Figure 1**a,b). In addition, the relatively thin (<100 µm) enol-**1** crystal can be bent slowly (≈s) only by UV light-induced photoisomerization. On the other hand, the $Ti_3C_2T_x$ layer-coated thin crystal can be bent rapidly (≈ms) by photothermal effect over a wide range of wavelengths (Figure 1c,d). The role of the $Ti_3C_2T_x$ layer in photothermal driving of molecular crystals is systemically studied through crystal monitoring, thermal imaging, and simulations under various conditions, and we also confirmed that $Ti_3C_2T_x$ hybridization can be extended to various types of molecular crystals. Moreover, the combination of the NIR light-induced actuation property and the high biocompatibility of the $Ti_3C_2T_x$-coated enol-**1** crystal allow the hybrid crystals to bend, even when they are enclosed or completely covered by agar phantoms that mimic biological tissue. This implies that the hybrid crystals actuated by broad-wavelength light have the potential to be applied as actuators in biological environments.

2. Results and Discussion

2.1. MXene for Photothermally Driven Crystal Actuation

MXene, an emerging novel family of 2D materials, also known as metal carbides, carbonitrides, and nitrides, have been spotlighted since its first discovery in 2011.[32–39] With a general formula of $M_{n+1}X_nT_x$ (n = 1–3), where M stands for early transition metals, X is C and/or N, and T_x is surface terminations such as —O, —OH, —F, and/or —Cl, MXene is known

© 2023 The Authors. Advanced Functional Materials published by Wiley-VCH GmbH

16163028, 2023, 47, Downloaded from https://onlinelibrary.wiley.com/doi/10.1002/adfm.202305916 by Koc University, Wiley Online Library on [05/02/2024]. See the Terms and Conditions (https://onlinelibrary.wiley.com/terms-and-conditions) on Wiley Online Library for rules of use; OA articles are governed by the applicable Creative Commons License

16163028, 2023, 47, Downloaded from https://onlinelibrary.wiley.com/doi/10.1002/adfm.202305916 by Koc University, Wiley Online Library on [05/02/2024]. See the Terms and Conditions (https://onlinelibrary.wiley.com/terms-and-conditions) on Wiley Online Library for rules of use; OA articles are governed by the applicable Creative Commons License

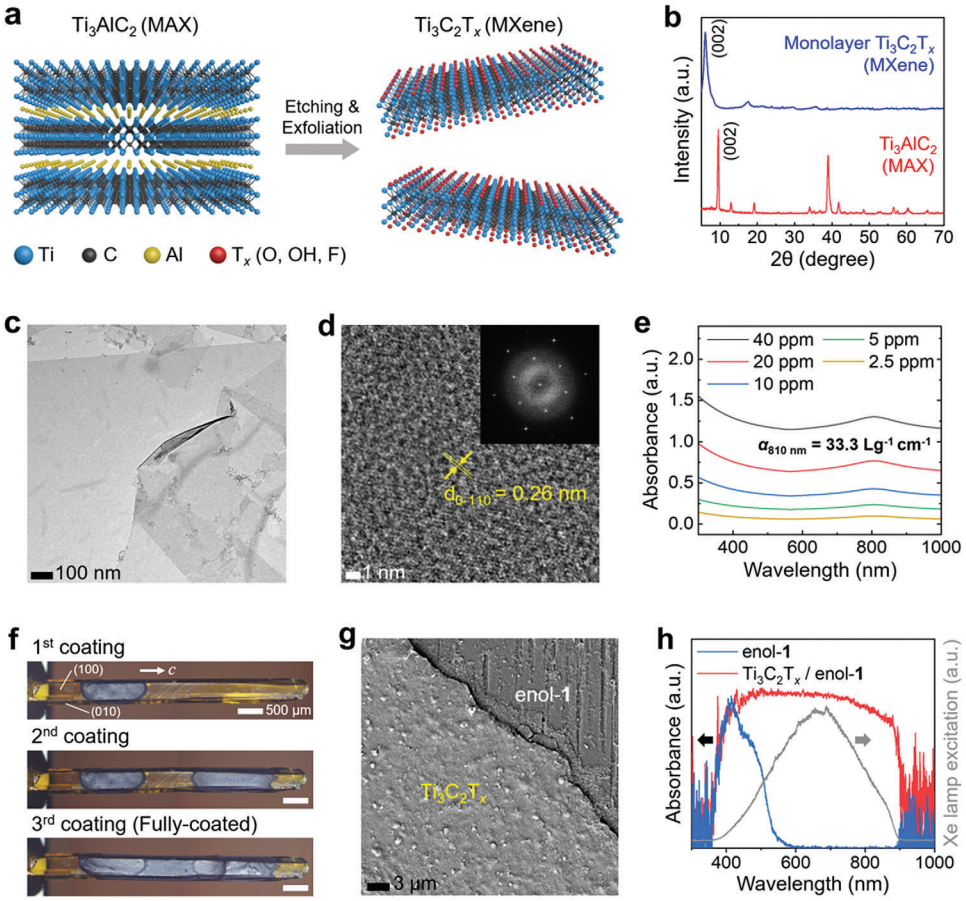


Figure 2. Preparation of $Ti_3C_2T_x$ MXene nanosheet and its coating on enol-1 crystal. a) Schematic of the $Ti_3C_2T_x$ MXene nanosheets preparation through Al etching and exfoliation of the MAX phase Ti_3AlC_2. b) XRD patterns of the exfoliated $Ti_3C_2T_x$ nanosheets and the Ti_3AlC_2 bulk powder. c) TEM image of the $Ti_3C_2T_x$ nanosheets. d) HRTEM image and SAED pattern (inset) of the $Ti_3C_2T_x$ nanosheet. e) UV–vis–NIR absorbance spectrum of the $Ti_3C_2T_x$ nanosheet-dispersed water solution with different concentrations. The extinction coefficient obtained at $\lambda = 810$ nm ($\alpha_{810\,nm}$) is also denoted. f) Digital photographs showing the coating process of the $Ti_3C_2T_x$ on the enol-1 crystal beam ($5251 \times 515 \times 246\ \mu m^3$) by three repetitive $Ti_3C_2T_x$ nanosheet solution drop-casting. g) SEM image showing the (100) plane of the $Ti_3C_2T_x$-coated enol-1 crystal. h) Absorbance spectrum of the pristine enol-1 crystal and the $Ti_3C_2T_x$-coated enol-1 crystal under excitation with Xenon (Xe) lamp light.

for its metallic conductivity,[32,33] photothermal effect,[34–36] and biocompatibility.[37,38] Among various MXene materials, we adopted titanium carbide ($Ti_3C_2T_x$), which is well-known for its excellent photothermal properties,[34–39] to generate photodynamic motion in molecular crystals. To prepare $Ti_3C_2T_x$, the MAX phase Ti_3AlC_2 was dissolved in a mixed solution of lithium fluoride (LiF) and hydrochloric acid (HCl) for 24 h followed by washing and exfoliation, where the Al atomic layer could be selectively etched to generate 2D Ti_3C_2 nanosheets. Simultaneously, —O, —OH, and —F surface terminations (T_x) were formed on the nanosheets to result in $Ti_3C_2T_x$ (**Figure 2**a; Figure S1, Supporting Information). The formation of monolayer $Ti_3C_2T_x$ was confirmed by X-ray diffraction (XRD) measurement (Figure 2b). After Al layer etching and nanosheet exfoliation, the (002) peak decreased from $2\theta = 9.54°$ (d-spacing = 0.93 nm) on Ti_3AlC_2 to $2\theta = 6.06°$ (d-spacing = 1.46 nm) on $Ti_3C_2T_x$. Also, the major peaks in bulk Ti_3AlC_2 were disappeared in $Ti_3C_2T_x$. These results show that the Al layer was successfully etched and the water molecules further exfoliated the prepared $Ti_3C_2T_x$ to form monolayered nanosheets.[34,39] Figure 2c and Figure S2, Supporting Information, exhibit transmission electron microscopy (TEM) images of the exfoliated $Ti_3C_2T_x$ MXene nanosheets with an average size of ≈2.36 ± 0.35 μm and an average thickness of ≈1.35 nm. The folded area at the edge of the nanosheet in Figure 2c demonstrates the high flexibility of $Ti_3C_2T_x$ nanosheets. The high-resolution TEM (HRTEM) image and selective area electron diffraction (SAED) pattern in Figure 2d indicate the hexagonal symmetry and single crystallinity of the prepared $Ti_3C_2T_x$ nanosheets with the lattice spacing of 0.26 nm which is indexed to the (0-110) plane.[40,41] The digital photographs of the aqueous $Ti_3C_2T_x$ nanosheet solution with typical Tyndall effect (Figure S3, Supporting Information) indicate their hydrophilicity and excellent dispersity.

The UV–vis–NIR absorption spectra acquired on the water solution of $Ti_3C_2T_x$ nanosheet showed its unique absorption in the NIR wavelength range from 750 to 850 nm (Figure 2e). The normalized absorption intensity (A) over the length of the cell (L) at $\lambda = 810$ nm at varied concentrations (C) (40, 20, 10, 5, and 2.5 ppm) was determined. According to the Lambert–Beer law ($A/L = \alpha C$, where α is the extinction coefficient), the linear dependence of

© 2023 The Authors. Advanced Functional Materials published by Wiley-VCH GmbH

A on *C* was obtained, and the α at 810 nm was measured to be 33.3 Lg^{-1} cm^{-1} (Figure S4, Supporting Information). This value was higher than that of reduced graphene oxide (24.6 Lg^{-1} cm^{-1}),[42] Au nanorods (13.9 Lg^{-1} cm^{-1}),[43] WS_2 nanosheets (23.8 Lg^{-1} cm^{-1}),[44] TiS_2 nanosheets (26.8 Lg^{-1} cm^{-1}),[45] MoS_2 nanosheets (29.2 Lg^{-1} cm^{-1}),[46] and Bi_2S_3 nanoflowers (20.5 Lg^{-1} cm^{-1}),[47] exhibiting the strong NIR absorption capability of $Ti_3C_2T_x$ MXene. In addition, the photothermal heat generation was observed in the $Ti_3C_2T_x$ aqueous solution droplets (10 μL, 50 mg mL^{-1}) upon irradiation with UV (365 nm), blue (455 nm), red (660 nm), and NIR (810 nm) light, and the photothermal conversion efficiency (η) was calculated based on the time constant for heat transfer and the maximum steady-state temperature (Note S1 and Figure S5, Supporting Information).[34] The calculated η for 365, 455, 660, and 810 nm wavelength were 62.9%, 21.4%, 55.9%, and 69.6%, respectively. The high η for NIR light that is comparable to that of high-energy UV light has been reported to originate from the localized surface plasmon resonance (LSPR) effect of the $Ti_3C_2T_x$ nanosheets.[32–39]

The $Ti_3C_2T_x$ layer was coated on the *p*-chlorosalicylideneaniline (enol-**1**) crystals[13] by drop-casting the $Ti_3C_2T_x$ nanosheets-dispersed water solution on the (001) top surface of the crystals (Figure 2f,g). Single plate-shaped yellow crystals of enol-**1** were readily obtained by acetone solution evaporation.[13] The crystal belongs to the monoclinic crystal system, and the *p*-chlorosalicylideneaniline molecules constituting the crystal are connected by short CH/O and CH/π contacts along the *c*-axis to form a longitudinal 1D motif, and the tert-butyl groups link the adjacent molecules along the *a*-axis through weak van der Waals forces (Figure S6, Supporting Information).[13] Due to the nonpolar tert-butyl groups on the (100) surface, the $Ti_3C_2T_x$ aqueous solution droplets maintained high contact angle (93.2°) on the crystal, and even after O_2-plasma treatment, contact angle only slightly decreased to 75.9° while maintaining high hydrophobicity (Figure S7, Supporting Information). Using the hydrophobicity of the crystal, we could monitor the changes in the photomechanical bending of the enol-**1** crystal according to the degree of coating by the $Ti_3C_2T_x$ layer. The tip of the relatively thick enol-**1** crystal (length (*L*): 5251 μm, width (*W*): 515 μm, thickness (*T*): 246 μm) was first fixed to the glass plate, and the (001) top plane of the enol-**1** crystal was coated with the $Ti_3C_2T_x$ layer by O_2-plasma treatment followed by successive $Ti_3C_2T_x$ solution drop-casting and evaporation (Figure 2f). Without O_2-plasma treatment, the droplets of the $Ti_3C_2T_x$ solution migrate toward the glass side or pipette tip rather than the crystals, making the entire coating difficult. After three successive coating processes, the (001) plane of the crystal was fully coated with a ≈1.3 μm-thick $Ti_3C_2T_x$ layer (Figure 2g; Figure S8 and Figure S9, Supporting Information).

The wavelength range of light absorbed by the pristine enol-**1** crystal and $Ti_3C_2T_x$-coated enol-**1** crystal was compared (Figure 2h). The thickness of the pristine enol-**1** and the $Ti_3C_2T_x$-coated enol-**1** crystal was 343 and 273 μm, respectively. The light from a Xenon (Xe) lamp having an emission wavelength of 400–900 nm was irradiated onto the crystal samples to obtain the absorbance spectra. The enol-**1** crystal only absorbed light in the range of 400–550 nm, but the $Ti_3C_2T_x$-coated enol-**1** crystal extended the absorption range of the crystal from 400 to 900 nm.

2.2. Photothermal Bending of MXene-Coated Crystals by Broad-Wavelength Light

Figure 3 shows the bending behavior of the $Ti_3C_2T_x$-coated enol-**1** crystal depending on the $Ti_3C_2T_x$ coating degree, wavelength of light, irradiation direction, and frequency of irradiation. The bending angle is defined as the difference between the bending-down displacement and the initial position. First, while irradiating UV light-emitting diode (LED) light (365 nm, 200 mW cm^{-2}) on the top (001) plane of the enol-**1** crystal, the change in bending behavior according to the degree of $Ti_3C_2T_x$ coating was observed (Figure 3a; Movie S1, Supporting Information). The enol-**1** crystal in Figure 2g was used for the test. The pristine enol-**1** crystal before $Ti_3C_2T_x$ layer coating started to bend immediately after UV light irradiation (< 0.1 s), bent to 0.52° at 0.8 s, and reached the maximum bending angle of 0.67° at 4.0 s. After the UV LED was turned off, the crystal immediately bent upward and returned to its original state. When the (001) plane of the same enol-**1** crystal started to be partially coated with $Ti_3C_2T_x$ layer through the first and second coating of the $Ti_3C_2T_x$ solution, the maximum bending angle by UV light irradiation decreased to 0.65° and 0.60°, respectively. The bending angle decreased to 0.56° when the crystal was fully coated with $Ti_3C_2T_x$ layer by the third coating. Second, when the (001) plane of the crystal was irradiated with NIR light (810 nm, 286 mW cm^{-2}) (Figure 3b; Movie S2, Supporting Information), the enol-**1** crystal showed no bending motion, indicating that enol-**1** has no absorption for NIR light, as already shown in Figure 2h. However, after the first $Ti_3C_2T_x$ partial coating, despite the coverage of 1/3 of the crystal area by $Ti_3C_2T_x$, the crystal started to bend in less than 0.1 s, bent to 0.23° at 0.4 s, and reached the maximum bending angle of 0.34° at 5.0 s. The secondary $Ti_3C_2T_x$ coating showed the similar result by slightly increasing the maximum bending angle to 0.36°, but when the entire crystal was coated with the $Ti_3C_2T_x$ layer, the maximum bending angle increased significantly to 0.55°. Another enol-**1** crystal with a slightly different geometry (*L*: 5043 μm, *W*: 493 μm, *T*: 255 μm) was also tested by changing the $Ti_3C_2T_x$ coating degree, and resulted in similar bending behavior, indicating the reproducibility of the experiment (Figure S10, Supporting Information).

In Figure 3c and Movie S3, Supporting Information, the change in the bending behavior of the $Ti_3C_2T_x$-coated enol-**1** crystal (*L*: 7560 μm, *W*: 914 μm, *T*: 256 μm) according to the wavelength of light was compared. The intensity of UV (365 nm), blue (455 nm), red (660 nm), and NIR (810 nm) LEDs was set to 200 mW cm^{-2}. By UV and NIR light irradiation, the crystal bent to 0.5° in less than 1.0 s and reached the maximum bending angle of 0.83°. The larger bending angle of the crystal in Figure 3c than in Figure 3a,b is due to the larger length-to-thickness ratio of the crystal compared to that used in Figure 3a,b.[16,48] The maximum bending angles by irradiation with blue and red visible light were 0.62° and 0.77°, respectively. The smaller bending angle of the crystal under red and blue light than under UV and NIR light is due to the smaller photothermal conversion efficiency of $Ti_3C_2T_x$ for visible light compared to UV and NIR light (Figure S5, Supporting Information), and this difference in photothermal effect will be further explained in **Figure 4**. To investigate the effect of the $Ti_3C_2T_x$ layer on the crystal bending at different wavelength, the $Ti_3C_2T_x$-coated crystal was flipped over and the uncoated bottom surface of the crystal was irradiated with light (Figure 3d–f;

© 2023 The Authors. Advanced Functional Materials published by Wiley-VCH GmbH

16163028, 2023, 47, Downloaded from https://onlinelibrary.wiley.com/doi/10.1002/adfm.202305916 by Koc University, Wiley Online Library on [05/02/2024]. See the Terms and Conditions (https://onlinelibrary.wiley.com/terms-and-conditions) on Wiley Online Library for rules of use; OA articles are governed by the applicable Creative Commons License

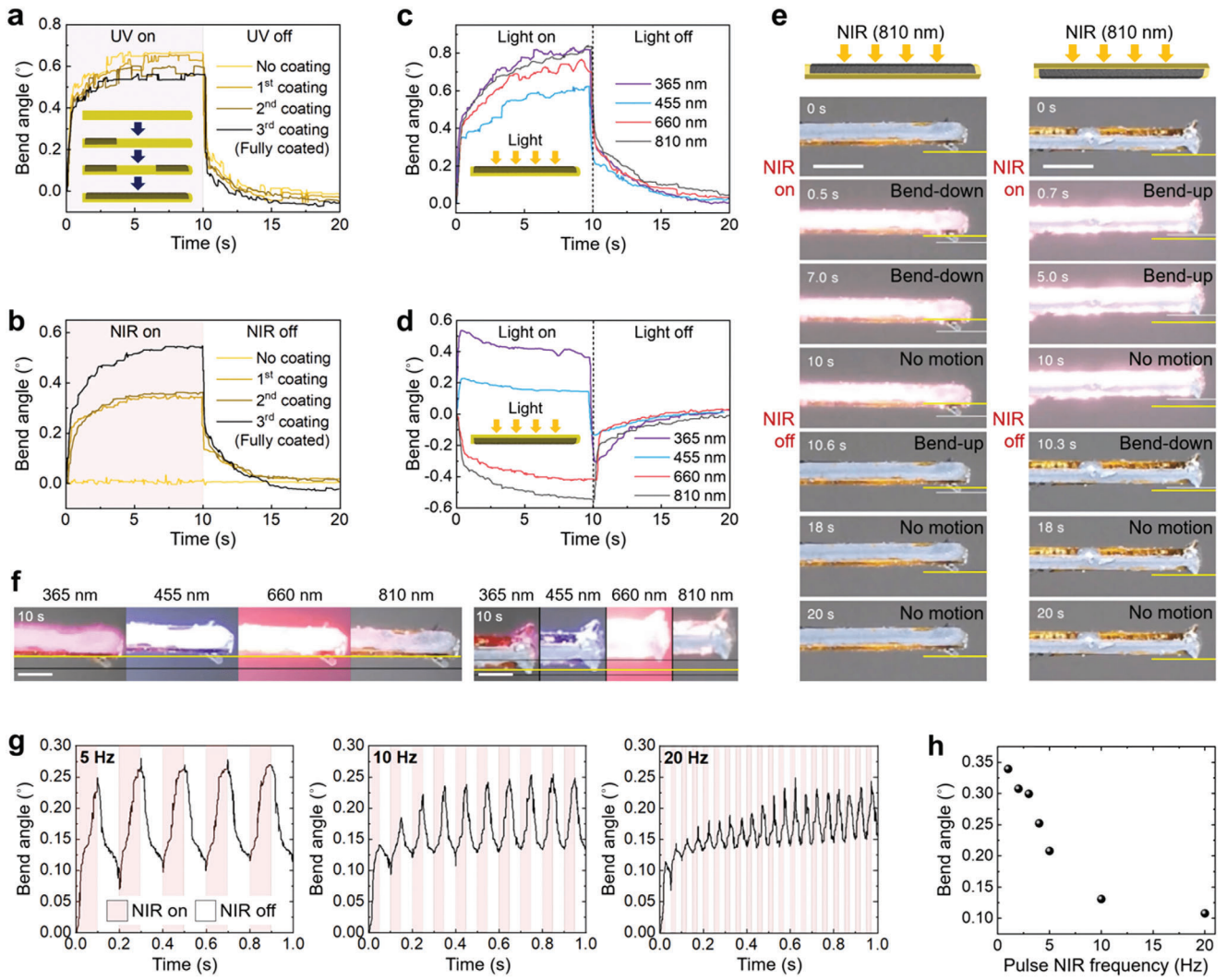


Figure 3. Bending of relatively thick $Ti_3C_2T_x$-coated enol-1 crystal beam upon light irradiation. a,b) Bending angle profiles of the Ti3C2Tx-coated enol-1 crystal beam (5251 × 515 × 246 μm3) according to the Ti3C2Tx coating degree (non-, partially-, and fully-coated). The crystal beam bending behavior was monitored upon UV (365 nm) (a) and NIR (810 nm) (b) LED irradiation. c,d) Bending angle profiles of the Ti3C2Tx-coated enol-1 crystal beam (7560 × 914 × 256 μm3) in non-flipped (c) and flipped (d) states. The LED is placed on top of the crystal, and light of different wavelength (365, 455, 660, and 810 nm) is illuminated to the top surface of the crystal. e,f) Side view snapshots of the non-flipped and flipped Ti3C2Tx-coated enol-1 crystal (the same crystal in (c,d)) that rapidly bends-down and bends-up upon irradiation of the NIR LED (e) and other wavelength LEDs (f). The yellow line is the initial position of the crystal tip and the scale bar in (e) and (f) are 500 and 250 μm, respectively. g) Profiles of the high-frequency crystal bending (5, 10, and 20 Hz, the same crystal in (c–f) by pulsed irradiation of the NIR (810 nm) LED. h) Change of peak-to-peak bending angle according to the frequency of pulsed NIR irradiation shown in (g).

Movie S4, Supporting Information). By UV and blue light irradiation, the flipped crystal immediately bent down and reached the maximum bending angle of 0.53° and 0.33° in less than 0.3 s, respectively. However, these bending angles were less than those of the non-flipped crystal (0.83° by UV and 0.62° by blue light). On the other hand, when the uncoated side of the flipped $Ti_3C_2T_x$-coated crystal was irradiated with red and NIR light, the crystal quickly bent to −0.25° and −0.33° and then reached −0.42° and −0.54°. This bend-up motion, opposite to the previous bend-down motion, indicates that red and NIR light are only absorbed by the $Ti_3C_2T_x$ layer and the temperature is increased by photothermal effect, forming a bottom-to-top temperature gradient.

The degree of bending behavior of the $Ti_3C_2T_x$-coated enol-1 crystal varied proportionally with the irradiation intensity of UV and NIR light (Figure S11, Supporting Information). When the UV irradiation intensity was gradually increased from 20 to 200 mW cm^{-2}, the maximum bending angle of the crystal gradually increased from 0.07° to 0.86° in the non-flipped state, and from 0.04° to 0.37° in the flipped state, respectively. The degree of the crystal bending by NIR also linearly followed the irradiation intensity. When the NIR irradiation intensity was gradually increased from 28.6 to 286 mW cm^{-2}, the maximum bending angle of the crystal gradually increased from 0.11° to 1.02° in the non-flipped state, and from −0.07° to −0.71° in the flipped state, respectively.

© 2023 The Authors. Advanced Functional Materials published by Wiley-VCH GmbH

16163028, 2023, 47, Downloaded from https://onlinelibrary.wiley.com/doi/10.1002/adfm.202305916 by Koc University, Wiley Online Library on [05/02/2024]. See the Terms and Conditions (https://onlinelibrary.wiley.com/terms-and-conditions) on Wiley Online Library for rules of use; OA articles are governed by the applicable Creative Commons License

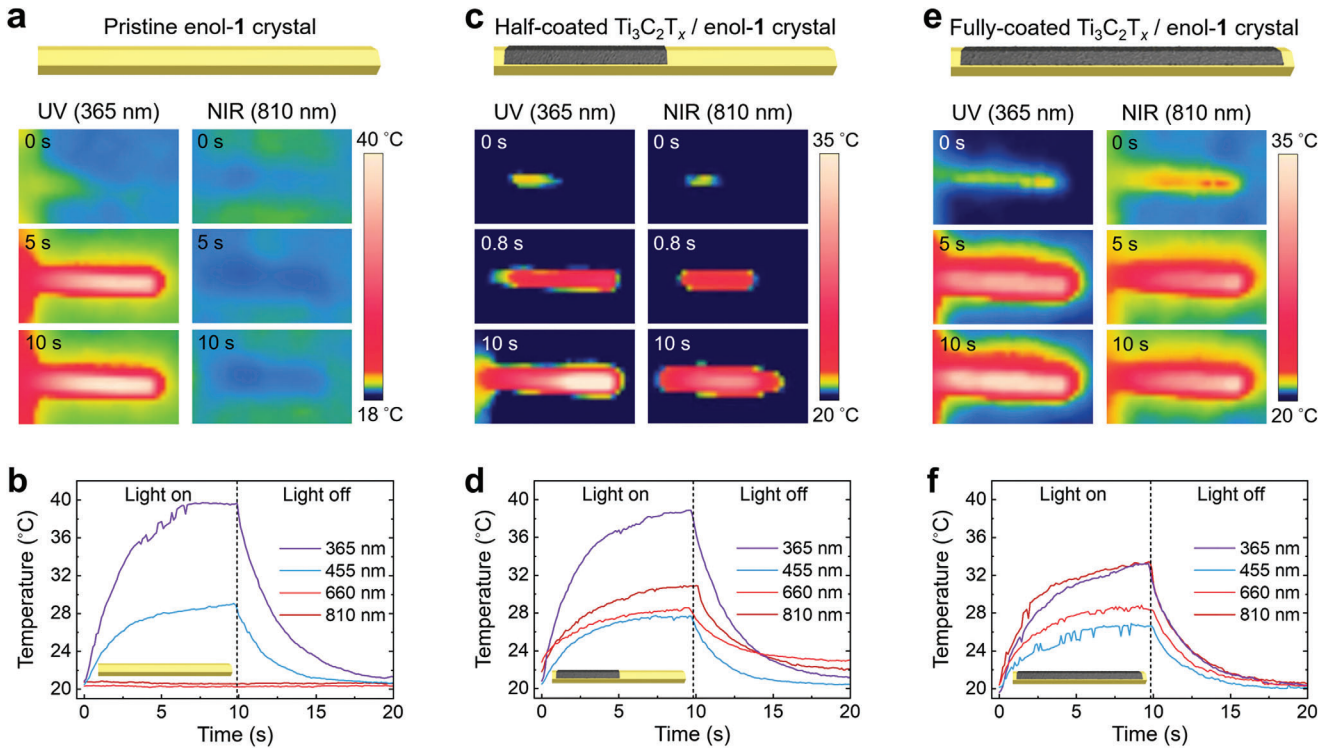


Figure 4. Photothermal heat generation on enol-**1** crystal and $Ti_3C_2T_x$-coated enol-**1** crystal beams. a,c,e) Infrared (IR) thermal images of the enol-**1** crystal (a), half-coated $Ti_3C_2T_x$/enol-**1** crystal (c), and fully-coated $Ti_3C_2T_x$/enol-**1** crystal (e) upon UV and NIR LED irradiation. Thermal imaging was performed while coating the $Ti_3C_2T_x$ on the same enol-**1** crystal, and each image shows the temporal temperature mapping of the light-irradiated area of the crystal. The number in the upper left indicates the time after starting LED irradiation. b,d,f) Time-dependent temperature change of the irradiated area of the pristine enol-**1** crystal (b), half-coated $Ti_3C_2T_x$/enol-**1** crystal (d), and fully-coated $Ti_3C_2T_x$/enol-**1** crystal (f) under irradiation with different wavelength of light. The LEDs of different wavelength are turned on and off for 10 s.

Next, high-frequency bending of the $Ti_3C_2T_x$-coated enol-**1** crystal by NIR light irradiation was examined (Figure 3g,h; Figure S12, Supporting Information). On/off pulsed irradiation of the NIR LED (810 nm, 290 mW cm^{-2}) was performed by the circuit controller. The frequency of NIR irradiation was adjusted from 1 to 2, 3, 4, 5, 10, and 20 Hz, and the bending behavior of the crystal was monitored. The crystal exhibited repeated bending higher than ≈0.2° until 5 Hz, and maintained repeated bending higher than ≈0.1° up to 20 Hz. At 0.5 Hz repeated irradiation, the reversible bending of the crystal was observed over 1000 cycles, maintaining the constant bending angle of ≈0.4° (Figure S13, Supporting Information), thus suggesting the high mechanical flexibility of the $Ti_3C_2T_x$ layer as well as the resilience and high durability of the crystal. The surface SEM images of the $Ti_3C_2T_x$ layer after 1000 cycles test are given in Figure S14, Supporting Information.

Furthermore, we investigated the correlation between the thickness of the $Ti_3C_2T_x$ layer and its bending performance (Figure S15, Supporting Information). To explore this relationship, we tested the same enol-**1** crystal with $Ti_3C_2T_x$ thicknesses of 780 nm and 1.74 µm by diluting the $Ti_3C_2T_x$ solution in coating process. Upon irradiation with the NIR LED (810 nm, 290 mW cm^{-2}), both crystal samples exhibited comparable bending degree and speed, achieving maximum bending angles of 0.54° (1.74 µm-thick sample) and 0.49° (780 nm-thick sample). The comparable bending performance of the crystals, irrespective of the thickness of the $Ti_3C_2T_x$ layer, can be attributed to the superior light-to-heat conversion efficiency of MXene and its high extinction coefficient at NIR wavelengths. In Figure 2f, we illustrated the formation of $Ti_3C_2T_x$ layer on the enol-**1** crystal. This was achieved by subjecting the (001) crystal plane to O_2-plasma treatment, followed by a step-wise drop-casting of the $Ti_3C_2T_x$ solution. To achieve a more uniform $Ti_3C_2T_x$ layer through a one-step solution coating process, we sputtered a thin layer of Au (20 nm-thick) onto the (001) plane of the crystal. The hydrophilicity of the Au layer facilitated the uniform coating of the $Ti_3C_2T_x$ layer across the entire crystal plane. The thickness of the $Ti_3C_2T_x$ layer in the /Au/enol-**1** hybrid crystal was also varied between 550 nm and 1.2 µm, and altering the $Ti_3C_2T_x$ layer thickness did not significantly affect the bending performance, similar to the $Ti_3C_2T_x$/enol-**1** crystal.

2.3. Photothermal Heat Generation of MXene-Coated Crystals

In Figure 4, temperature change of the pristine enol-**1** and $Ti_3C_2T_x$-coated enol-**1** crystal was monitored during LED irradiation (86.4 mW cm^{-2}) to explain the bending behavior of the crystal in Figure 3 and reveal the role of the $Ti_3C_2T_x$ layer in the photothermally driven crystal actuation. The time-dependent temperature change of the (001) plane of the enol-**1** crystal (*L*: 4236 µm, *W*: 633 µm, *T*: 478 µm) was observed using an infrared

© 2023 The Authors. Advanced Functional Materials published by Wiley-VCH GmbH

16163028, 2023, 47, Downloaded from https://onlinelibrary.wiley.com/doi/10.1002/adfm.202305916 by Koc University, Wiley Online Library on [05/02/2024]. See the Terms and Conditions (https://onlinelibrary.wiley.com/terms-and-conditions) on Wiley Online Library for rules of use; OA articles are governed by the applicable Creative Commons License

16163028, 2023, 47, Downloaded from https://onlinelibrary.wiley.com/doi/10.1002/adfm.202305916 by Koc University, Wiley Online Library on [05/02/2024]. See the Terms and Conditions (https://onlinelibrary.wiley.com/terms-and-conditions) on Wiley Online Library for rules of use; OA articles are governed by the applicable Creative Commons License

(IR) thermal imaging camera (Figure 4a,b; Movie S5, Supporting Information). When the enol-**1** crystal was irradiated with UV (365 nm) light, the temperature of the (001) plane rose from 20.8 °C and reached 39.6 °C in 10 s. Similarly, blue (455 nm) LED irradiation increased the temperature of the enol-**1** crystal surface from 20.5 to 28.9 °C in 10 s. However, red (660 nm) and NIR (810 nm) LED irradiation made no temperature change to the enol-**1** crystal, indicating that enol-**1** has no absorption for red and NIR wavelength. In Figure 4c,d and Movie S6, Supporting Information, the left half (001) plane of the same crystal was coated with $Ti_3C_2T_x$ layer, and the temperature profile was obtained during light irradiation. Before LED irradiation, the $Ti_3C_2T_x$ coated area showed a slightly higher temperature (≈21 °C) than the background because IR rays from the thermal imaging camera or white light from the optical microscope could be absorbed by the $Ti_3C_2T_x$ layer. When the half-coated crystal was irradiated with UV and blue LED, the heat was generated on the whole area of the (001) crystal plane, and the temperature reached at maximum of 38.9 and 27.7 °C in 10 s, respectively. These UV and blue light-induced temperature increases were similar to that of the pristine enol-**1** crystal, but the maximum temperature on the non-coated enol-**1** area (right) of the crystal was higher than the $Ti_3C_2T_x$-coated area (left). Upon NIR light irradiation, the temperature of the $Ti_3C_2T_x$-coated area increased (28.0 °C in 3 s), and at the same time, it can be clearly observed that the heat generated in the $Ti_3C_2T_x$ area propagates to the right enol-**1** area by immediate thermal conduction. The maximum temperature of the half $Ti_3C_2T_x$-coated enol-**1** crystal reached by red and NIR LED irradiation for 10 s was 28.5 and 30.9 °C, respectively. Figure 4e,f, and Movie S7, Supporting Information show the time-dependent temperature change of the fully-coated $Ti_3C_2T_x$/enol-**1** crystal by irradiation of different wavelength of light. By UV and blue light irradiation, heat was generated on the $Ti_3C_2T_x$-coated (001) crystal plane, but the maximum temperature reached at 10 s (33.2 °C by UV and 26.6 °C by blue light) was smaller than that of enol-**1** and half-coated $Ti_3C_2T_x$/enol-**1** crystal. These results indicate that the $Ti_3C_2T_x$ layer has lower absorption and photothermal effect for UV and blue light than that of the enol-**1** crystal, and the blocking of UV and blue light on the enol-**1** surface by $Ti_3C_2T_x$ layer reduces the photothermal heat generation of enol-**1** crystal. However, for red and NIR light irradiation, the photothermal heating by $Ti_3C_2T_x$ layer increased the surface temperature to 28.8 and 33.2 °C, respectively. Additionally, the relationship between the degree of photothermal heating and the degree of bending of the $Ti_3C_2T_x$/enol-**1** crystal was investigated according to the wavelength. The heat generation of the $Ti_3C_2T_x$/enol-**1** crystal used in Figure 2c–e was monitored as a function of wavelength (Figure S16, Supporting Information). The difference in temperature increases of the crystal during UV, blue, red, and NIR light irradiation had the similar tendency with the difference of the bending angles, confirming that the bending degree is highly related to the photothermal effect of $Ti_3C_2T_x$.

2.4. Bending of MXene-Coated Thin Crystals by Photothermal Effect

According to our previous study of enol-**1** crystal,[13] unlike the relatively thick (T > 100 μm) enol-**1** crystals that bent away quickly through photothermal effect upon UV and blue light irradiation, the relatively thin (T < 33 μm) enol-**1** crystals showed gradual bend-up motion toward the UV light source and slow recovery to the original states due to the UV-induced photoisomerization, and the slightly thick crystals (T: 33–100 μm) exhibited two-step bending through both photothermal effect and photoisomerization.[13] Photoisomerization negligibly affects the bending of thicker crystals (T > 100 μm) because the strain generated by photoreacted molecular layer (3.54 μm)[13] on the irradiated surface cannot be effectively translated into macroscopic bending for thicker crystals. We confirmed these changes in bending behavior with crystal thickness by irradiating UV light to the enol-**1** crystals with two different thickness (T: 30 and 60 μm) (**Figure 5**a; Figure S17 and Movie S8, Supporting Information). Upon UV light irradiation (365 nm, 200 mW cm^{-2}), the 30 μm-thick enol-**1** crystal (L: 6811 μm, W: 482 μm, T: 30 μm) showed very weak bend-down motion at the beginning (0.04° at 0.03 s) but then gradually bent up to −1.76° over 10 s. Then, when the UV LED was off, it slowly bent down toward the initial position and reached −0.1° after 138 s was passed. In case of the 60 μm-thick enol-**1** crystal (L: 1889 μm, W: 242 μm, T: 60 μm), the crystal showed immediate bend-down motion (0.2° at 0.07 s) when the UV light was turned on, and then it bent up toward the UV LED and reached −1.24° at 10 s. When the UV light was turned off at 10 s, the bending angle suddenly increased from −1.24° to −1.69°, and the crystal slowly returned to initial position (0°) at 148 s. Both 30 μm- and 60 μm-thick enol-**1** crystals showed no motions upon visible and NIR light irradiation (Figure S17, Supporting Information). The schematic diagram in Figure 5c exhibits the mechanism for the UV light-induced bending of the thin enol-**1** crystal. Upon UV light irradiation, the crystal bends down away from the UV light source through the immediate photothermal effect-induced temperature gradient (ΔT). However, as enol-to-keto photoisomerization of the molecules near the irradiated surface starts, the crystal bends up toward the light source because the *trans*-keto photoproducts generate the mechanical strain. When UV light is off, the temperature gradient formed in the crystal by photothermal effect becomes rapidly relaxed, and the gradual keto-to-enol back-isomerization returns the crystal to its initial state slowly. Since the thicker the enol-**1** crystal, the less the influence of the photoisomerization-reacted surface layer and the more predominantly photothermal effect is applied, the 60 μm-thick enol-**1** crystal showed the clear photothermal effect-induced bend-down motion than the 30 μm-thick crystal, as well as smaller photoisomerization-induced maximum bend-up angle. The sharp increase in the negative bending angle when the UV light was turned off in the 60 μm-thick enol-**1** crystal is due to the immediate relaxation of photothermal effect and the simultaneous increase in the strain gradient within the crystal.

In Figure 5b and Movie S9, Supporting Information, bending behavior of the $Ti_3C_2T_x$-coated thin enol-**1** crystal (L: 1242 μm, W: 172 μm, T: 27 μm) was monitored upon light irradiation of UV (365 nm), blue (455 nm), red (660 nm), and NIR (810 nm) wavelength. Similar to the results on thick crystals (Figure 3c), the crystal under NIR light showed the larger bending motion (0.71° at 1.0 s, maximum of 0.90° at 4.4 s) than under red (0.56° at 1.0 s, maximum of 0.62° at 4.0 s) and blue (0.44° at 1.0 s, maximum of 0.55° at 4.2 s) light irradiation. Upon UV light irradiation, this crystal also showed bend-down motion, but the slower increase

© 2023 The Authors. Advanced Functional Materials published by Wiley-VCH GmbH

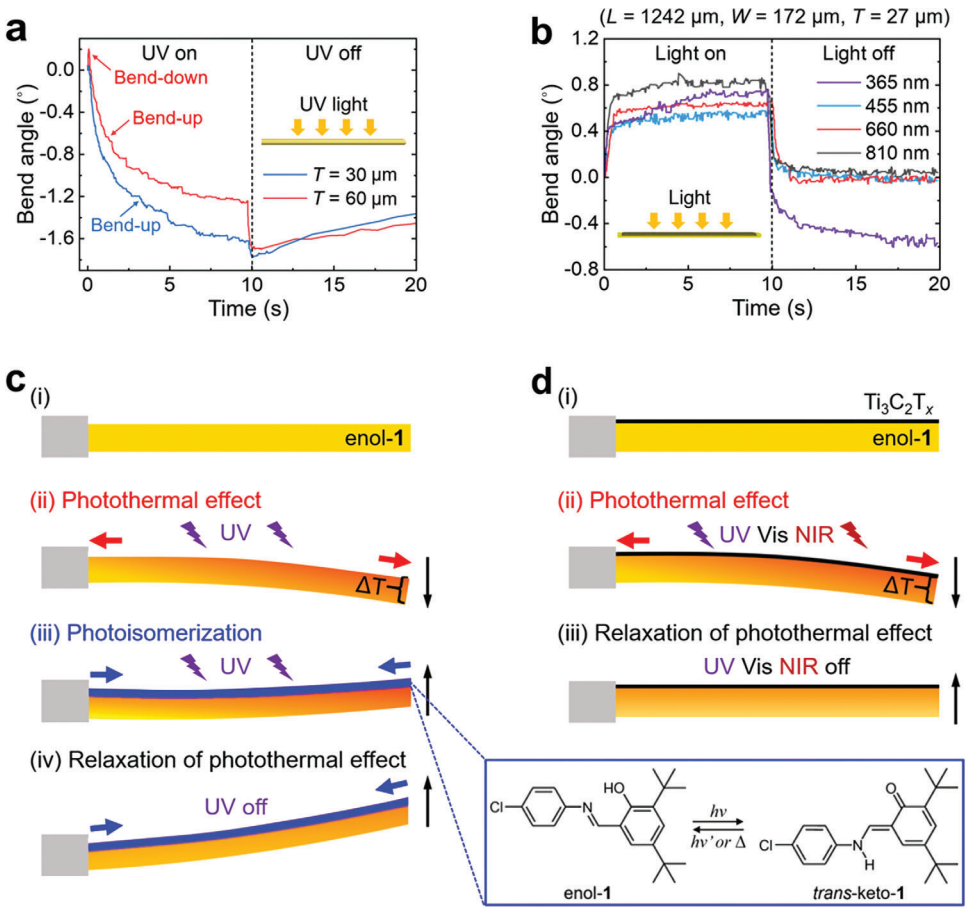


Figure 5. Bending of relatively thin $Ti_3C_2T_x$-coated enol-**1** crystal upon light irradiation. a) Bending angle profiles of two thin enol-**1** crystal beams (6811 × 482 × 30 μm^3 and 1889 × 242 × 60 μm^3 upon UV light (365 nm) irradiation. b) Bending angle profile of the $Ti_3C_2T_x$-coated thin enol-**1** crystal beam (1242 × 172 × 27 μm^3) under irradiation with different wavelength of light. c,d) Schematic diagram showing the bending mechanism of thin enol-**1** crystal beam (c) and $Ti_3C_2T_x$-coated thin enol-**1** crystal beam (d).

of bending angle (0.49° at 1.0 s, maximum of 0.76° at 6.3 s) compared to other three wavelength. Also, when the UV light was turned off, the crystal showed gradual bend-up motion by reaching −0.57° at 20 s which is similar to the photoisomerization-induced bending in the pristine enol-**1** crystals.

To investigate more on the UV light-induced bending of the $Ti_3C_2T_x$-coated thin enol-**1** crystal, another enol-**1** crystal of different geometry (*L*: 1312 μm, *W*: 213 μm, *T*: 56 μm) was coated with $Ti_3C_2T_x$ layer and tested for bending (Figure S18, Supporting Information). This crystal showed maximum bending angle of 0.24°, 0.12°, 0.10° upon NIR, red, and blue light, respectively, which are smaller than the one in Figure 5b. Upon UV light irradiation, the crystal immediately bent down by 0.2° but then gradually bent up with a behavior similar to the enol-**1** crystal in Figure 5a. The degree of bending is mainly related to the crystal thickness (*T*), rather than length (*L*) or width (*W*), since thickness is a component of second moment of inertia (I, $I = \frac{WT^3}{12}$) with third order, and thus the increase in thickness significantly increases the resistance to bending.[48] From these results, we can say that thin $Ti_3C_2T_x$-coated enol-**1** crystals with a thickness of less than 100 μm can be bent only by photothermal effect under visible and NIR light (Figure 5d). However, when irradiated with UV light, photoisomerization can also affect bending, and the degree of its effect depends on the crystal dimension.

2.5. Simulation of Photothermally Driven Bending of MXene-Coated Crystals

Upon photoirradiation to crystals, heat was generated from the light-absorbing layer and conducts into the thickness direction. As a result, the temperature gradient is formed in the thickness direction, and the non-steady thermal elongation difference between the top and back surfaces leads the photothermally driven bending.[16] To understand the differences among UV, visible, and NIR light-induced bending based on photothermal effect and heat conduction, bending simulations of the non-flipped and flipped $Ti_3C_2T_x$-coated enol-**1** crystals were conducted using a finite element method. First, the 2D geometries of the cross-section surface of the same crystal as Figure 3c,d was designed, and the photothermally generated heat was applied as heat flux values on $Ti_3C_2T_x$ and enol-**1** layers as shown in Figure S19 and S20, Supporting Information, by considering the photothermal conversion efficiency (Figure S5, Supporting Information)

© 2023 The Authors. Advanced Functional Materials published by Wiley-VCH GmbH

16163028, 2023, 47, Downloaded from https://onlinelibrary.wiley.com/doi/10.1002/adfm.202305916 by Koc University, Wiley Online Library on [05/02/2024]. See the Terms and Conditions (https://onlinelibrary.wiley.com/terms-and-conditions) on Wiley Online Library for rules of use; OA articles are governed by the applicable Creative Commons License

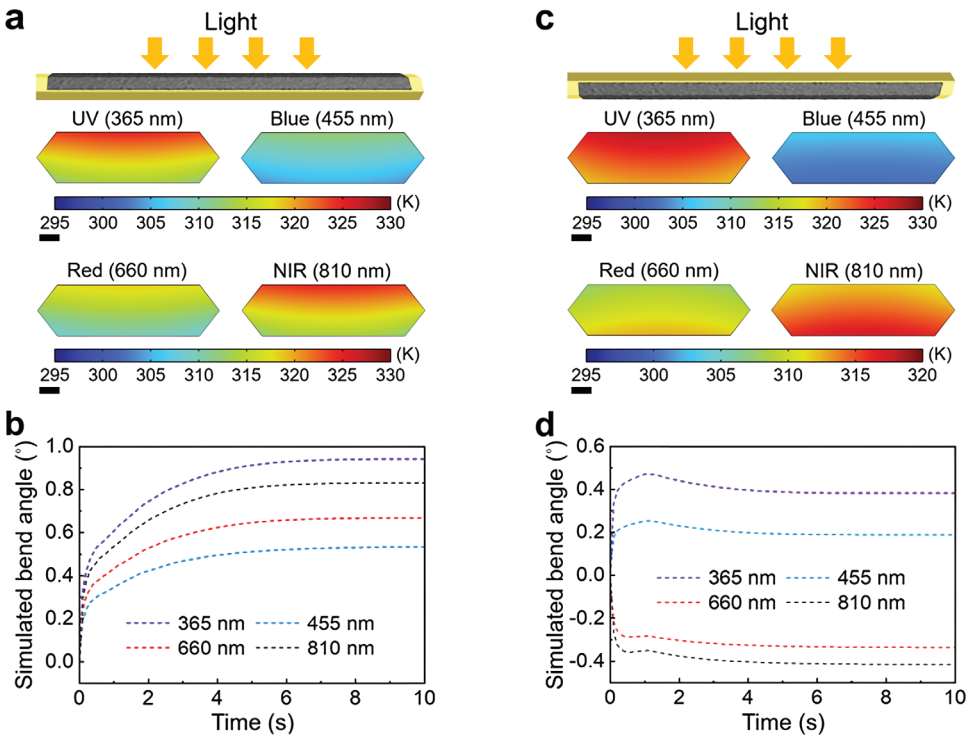


Figure 6. Simulation of photothermally driven $Ti_3C_2T_x$-coated enol-**1** crystal bending. Bending simulation of the fully-coated $Ti_3C_2T_x$/enol-**1** crystal (7560 × 914 × 256 μm^3) in non-flipped (a,b) and flipped (c,d) states based on the non-steady heat conduction using finite element method. a,c) Simulated temperature distribution after UV (365 nm), blue (455 nm), red (660 nm), and NIR (810 nm) LED irradiation for 10 s (Scale bar: 100 μm). b,d) Time dependence of simulated bending angles under UV (365 nm, purple dot curve), blue (455 nm, blue dot curve), red (660 nm, red dot curve), and NIR (810 nm, grey dot curve).

and the absorption spectra in Figure 2e,h. Then, the temperature gradient was calculated based on the non-steady heat conduction as:

$$\frac{\partial T(x,\ t)}{\partial t} = \frac{k}{\rho C_p}\frac{\partial^2 T(x,\ t)}{\partial x^2} - h\left(T(x,\ t) - T_{\text{air}}\right) \quad (1)$$

where $T(x, t)$ is the temperature at a certain displacement x along the thickness direction and a time t, k is the heat conduction, C_p is the specific heat capacity, h is the heat transfer coefficient, and T_{air} is the atmospheric temperature. The bending angle θ is calculated by using the simulated temperature difference ΔT between top and back surfaces:[16]

$$\theta = \frac{a\Delta TL}{2d} \quad (2)$$

where a is the thermal expansion coefficient along the length direction (77.0 MK^{-1} in enol-**1** crystals),[13] L is the crystal length (7560 μm), and d is the crystal thickness (256 μm).

In the non-flipped state, the maximum top surface temperature was calculated to 329, 307, 319, and 325 K upon UV, blue, red, and NIR LED irradiation for 10 s, respectively. This difference of temperature increase in each wavelength matches well with the experimental results (Figure 4f; Figure S16b, Supporting Information). By conduction of the photothermally generated heat, the simulated temperature gradient was uniformly formed into the thickness direction in all results of **Figure 6**a and Movie S10, Supporting Information. From the simulated temperature difference between the simulated temperatures of the top and back surfaces (Figure S21, Supporting Information), the simulated bending angle reached to 0.94° (365 nm), 0.37° (455 nm), 0.67° (660 nm), and 0.83° (810 nm) at the maximum (Figure 6b). These maximum angles match well to those in Figure 3c. Also, the time profiles of simulated bending can be fitted to the bi-exponential curves, dividing the faster and the slower components. The time constants of the faster component were estimated to 0.066 s (365 nm), 0.067 s (455 nm), 0.063 s (660 nm), and 0.063 s (810 nm), which are also comparable to the time profiles in Figure 3c (Figure S23 and Table S2, Supporting Information).

In the flipped state, the crystal temperature reached the maximum values of 320 and 313 K on the top surface upon UV and blue LED irradiation for 10 s, respectively (upper two figures in Figure 6c). In contrast, upon red and NIR light irradiation for 10 s, the maximum temperatures (307 and 317 K, respectively) were located on the back surface. As a result, UV and blue light induced the temperature gradient from the top to the back surface, on contrary, red and NIR light led the temperature gradient from the back to the top surface (Figure 6c; Figure S22 and Movie S11, Supporting Information). The bending behavior was also changed between UV and blue light, and red and NIR light. Upon UV and blue light, the bending angles once reached to the maximum value (0.47° and 0.25°, respectively) in ≈1.0 s, and then slightly decreased to be the stable angle of 0.38° and 0.19°, respectively (Figure 6d). By red and NIR light irradiation for 10 s, the

© 2023 The Authors. Advanced Functional Materials published by Wiley-VCH GmbH

16163028, 2023, 47, Downloaded from https://onlinelibrary.wiley.com/doi/10.1002/adfm.202305916 by Koc University, Wiley Online Library on [05/02/2024]. See the Terms and Conditions (https://onlinelibrary.wiley.com/terms-and-conditions) on Wiley Online Library for rules of use; OA articles are governed by the applicable Creative Commons License

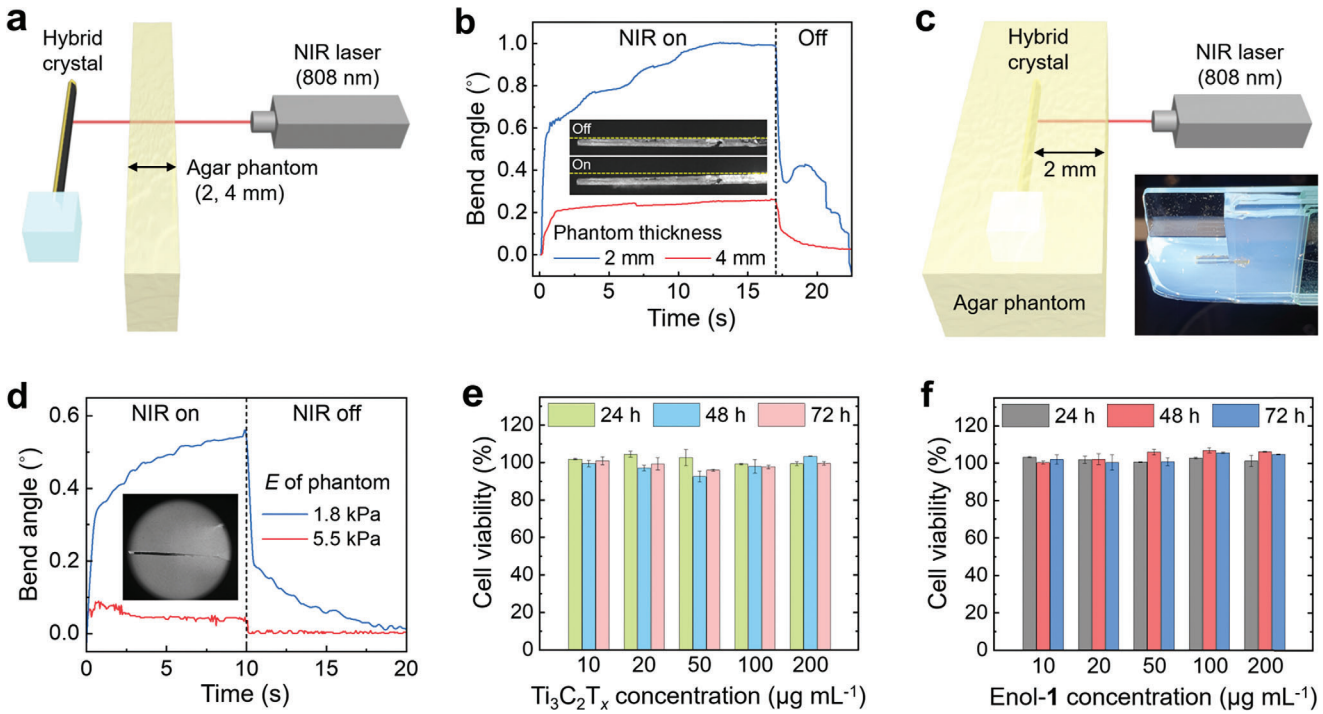


Figure 7. NIR light-induced bending of $Ti_3C_2T_x$-coated enol-**1** crystal inside a tissue-like phantom. a) Schematic experimental setup for testing the NIR light-driven bending of the $Ti_3C_2T_x$-coated enol-**1** crystal surrounded by agar phantoms of different thicknesses of wall. b) Bending angle profiles of the $Ti_3C_2T_x$-coated enol-**1** crystal beam (1312 × 213 × 56 μm^3) according to the agar phantom wall thickness. Inset photograph shows the crystal bent by irradiated laser beam passed through the agar phantom wall (2.0 mm-thick). c) Schematic experimental setup for testing the NIR light-driven bending of the $Ti_3C_2T_x$-coated enol-**1** crystal inside agar phantoms. Inset photograph shows the crystal inside the agar phantom. d) Bending angle profiles of the $Ti_3C_2T_x$-coated enol-**1** crystal beam (4951 × 388 × 190 μm^3) according to the Young's modulus (*E*) of agar phantom. e,f) Viability of fibroblasts cells exposed to various concentrations of $Ti_3C_2T_x$ nanosheets (e) and enol-**1** crystals (before crystal beams formation) (f) for 24, 48, and 72 h.

crystal bent up to reach the minimum bending angle to −0.34° and −0.41°, respectively (Figure 6d). These simulated results are also fitted to the bi-exponential curves and are roughly coincident with the experimental bending in Figure 3d (Figure S24 and Table S2, Supporting Information). Therefore, by considering light absorption, photothermal energy conversion, and heat conduction, the bending behavior difference in each wavelength and state could be reproduced, and existence of $Ti_3C_2T_x$ layer is confirmed to play a key role for determining motion and direction of the photothermally driven bending.

2.6. Actuation of Hybrid Crystals inside Tissue-Like Phantoms

Actuation of the $Ti_3C_2T_x$-coated enol-**1** crystal under NIR light enables photothermal crystal actuation inside a tissue-like phantom. First, we conducted test to determine the feasibility of actuation in water. However, upon immersing the $Ti_3C_2T_x$-coated crystal in water, the coated $Ti_3C_2T_x$ became detached from the crystal and dispersed into the water (Figure S25, Supporting Information). Therefore, we employed agar phantoms, commonly used to imitate soft tissue[49] to observe the NIR (808 nm) light-induced bending of the $Ti_3C_2T_x$-coated enol-**1** hybrid crystal. The hybrid crystals were tested by placing them adjacent to the agar wall and also being encapsulated inside the agar phantom. **Figure 7**a shows a schematic of the experimental setup for testing the NIR light-driven actuation of the hybrid crystals placed adjacent to the agar phantom (1.4 wt%) walls of different thicknesses. The average Young's modulus of the agar phantom was 1.8 kPa that are similar to the range of endothelial tissue or brain.[50] The $Ti_3C_2T_x$-coated region of the hybrid crystal (*L*: 1312 μm, *W*: 213 μm, *T*: 56 μm) was irradiated with a NIR laser (808 nm, 500 mW), and the change of the crystal bending angle according to the thickness of the agar phantom wall was monitored by a top-mounted high-speed camera. Even when there was a 2.0 mm-thick agar phantom wall separating the crystal and laser, the crystal bent to a maximum of 1.0° after bending to 0.60° in less than a second (Figure 7b and Movie S12, Supporting Information). However, when the thickness of agar phantom was increased to 4.0 mm, the maximum bending angle reduced to 0.21°, respectively, but the high bending speed of the crystal remained consistent.

In Figure 7c,d, Figure S26 and Movie S12, Supporting Information, we tested the actuation of $Ti_3C_2T_x$-coated enol-**1** hybrid crystal by completely covering it with the agar phantom (1.4 and 3.0 wt%). After immersing the hybrid crystal with the agar phantom following its curing at room temperature, we cut the half left of the phantom to monitor the movement of the crystal with a high-speed camera (Figure S26, Supporting Information). The distance from the crystal to the end of the agar phantom was set as 2.0 mm. Despite being covered in the agar phantom (1.4 wt%), the crystal (*L*: 4951 μm, *W*: 388 μm, *T*: 190 μm) bent to a maximum bending angle of 0.55°, although it took longer to reach the

© 2023 The Authors. Advanced Functional Materials published by Wiley-VCH GmbH

16163028, 2023, 47, Downloaded from https://onlinelibrary.wiley.com/doi/10.1002/adfm.202305916 by Koc University, Wiley Online Library on [05/02/2024]. See the Terms and Conditions (https://onlinelibrary.wiley.com/terms-and-conditions) on Wiley Online Library for rules of use; OA articles are governed by the applicable Creative Commons License

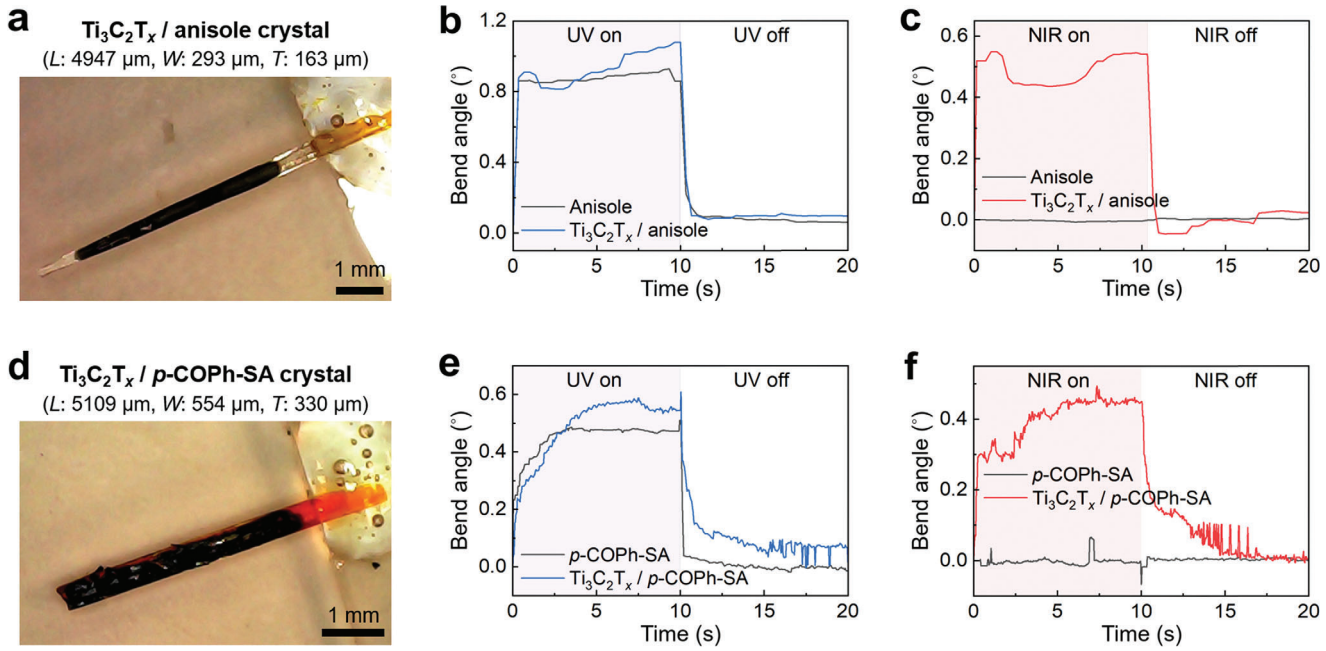


Figure 8. Extension of the $Ti_3C_2T_x$ effect to various photothermally driven crystal actuators. a) Photograph of the relatively thick $Ti_3C_2T_x$-coated anisole crystal cantilever beam. b,c) Bending angle profiles of the $Ti_3C_2T_x$-coated anisole crystal beam (4947 × 293 × 163 μm^3) according to the $Ti_3C_2T_x$ coating. The crystal beam bending behavior was monitored upon UV (375 nm) (b) and NIR (808 nm) (c) LED irradiation. d) Photograph of the relatively thick $Ti_3C_2T_x$-coated *p*-COPh-SA crystal cantilever beam. e,f) Bending angle profiles of the $Ti_3C_2T_x$-coated *p*-COPh-SA crystal beam (5109 × 554 × 330 μm^3) according to the $Ti_3C_2T_x$ coating. The crystal beam bending behavior was monitored upon UV (375 nm) (e) and NIR (808 nm) (f) LED irradiation.

maximum bending angle and return to the original state compared to when it was tested in air. However, when the modulus of the high-concentration agar phantom (3.0 wt%) increased to 5.5 kPa, the actuation of the crystal was restricted. This can be attributed not only to the high modulus of the agar phantom, but also to the reduced transparency of the phantom, which scatters the NIR laser beam and reduces the crystal's ability to generate photothermal heat.

In addition, we tested the cytotoxicity of the *p*-chlorosalicylideneaniline (enol-**1**) molecular crystals and $Ti_3C_2T_x$ MXene nanosheets with fibroblast cells (Figure 7e,f). Different concentrations (10–200 μg mL^{-1}) of two different materials were incubated with fibroblast cells, and their viability was investigated for up to 72 h. After 72 h incubation with $Ti_3C_2T_x$ and enol-**1**, the viability of fibroblasts was more than 95% in all treated groups, implying that the hybrid crystal actuators are biocompatible and safe to use in biological environments. Lastly, to evaluate the stability of agar-encapsulated $Ti_3C_2T_x$/enol-**1** crystals in biological environments, we immersed the agar phantom-encapsulated hybrid crystals in two biological media, namely, Dulbecco's phosphate-buffered saline (DPBS) and Dulbecco's modified eagle's medium (DMEM)[51,52] and monitored any changes that occurred in the samples. DPBS closely mimics the pH, osmolality, and ion concentrations of the human body, while DMEM is a widely used basal medium to support the growth of a variety of cells. The $Ti_3C_2T_x$-coated enol-**1** crystal within the agar phantom exhibited high stability, remaining intact for 24 h in both the DPBS and DMEM media (Figure S27, Supporting Information).

2.7. Applicability to Various Photothermally Driven Crystal Actuators

Extending the range of light wavelengths capable of driving photothermal actuation in molecular crystals through $Ti_3C_2T_x$ MXene coating holds great potential for application across various types of crystals. In addition to testing the *p*-chlorosalicylideneaniline (Enol-**1**) crystal, we also conducted tests on two other molecular crystals; 2,4-dinitroanisole (Anisole)[53] and *N*-3,5-di-tert-butylsalicylidene-4-benzoylaniline (*p*-COPh-SA)[15] (**Figure 8**). Coating the thick anisole crystal (4947 × 293 × 163 μm^3) with the $Ti_3C_2T_x$ solution results in a uniform $Ti_3C_2T_x$ layer on the crystal (Figure 8a). Under the UV LED (375 nm, 350 mW cm^{-2}) irradiation, the anisole crystal exhibited fast bending (up to 0.9°–1.0°) and recovery behavior regardless of $Ti_3C_2T_x$ layer coating (Figure 8b). The pristine anisole crystal showed no motions under the NIR LED (808 nm, 350 mW cm^{-2}) irradiation, but the $Ti_3C_2T_x$/anisole hybrid crystal bent down immediately, reaching the maximum bending angle of 0.54° within 0.2 s, and recovered to its initial state within 1.0 s after the LED was turned off (Figure 8c). The *p*-COPh-SA crystal (5109 × 554 × 330 μm^3), which is an another salicylideneaniline derivative with a *p*-benzoyl substituent underwent the same bending test before and after $Ti_3C_2T_x$ layer coating (Figure 8d). The *p*-COPh-SA crystal showed similar bending behavior under UV light irradiation before and after coating, but only the $Ti_3C_2T_x$/*p*-COPh-SA hybrid crystal showed comparable bending behavior under NIR light (Figure 8e,f).

© 2023 The Authors. Advanced Functional Materials published by Wiley-VCH GmbH

16163028, 2023, 47, Downloaded from https://onlinelibrary.wiley.com/doi/10.1002/adfm.202305916 by Koc University, Wiley Online Library on [05/02/2024]. See the Terms and Conditions (https://onlinelibrary.wiley.com/terms-and-conditions) on Wiley Online Library for rules of use; OA articles are governed by the applicable Creative Commons License

3. Conclusion

In summary, through hybridization of *p*-chlorosalicylideneaniline (enol-**1**) molecular crystals with $Ti_3C_2T_x$ MXene nanosheets, the broad-wavelength (UV, visible, and NIR) light-driven crystals exhibiting fast photothermally driven macroscopic bending were developed. Compared to the relatively thick enol-**1** crystals, which can be bent only by photothermal heat generation upon UV and blue light irradiation, and the relatively thin crystals which are bent slowly by UV-induced photoisomerization, the $Ti_3C_2T_x$ layer coated on the enol-**1** crystals enabled fast and effective crystal bending regardless of the crystal thickness. The $Ti_3C_2T_x$-coated enol-**1** crystals showed relatively larger bending under UV and NIR light than visible light, and also, the bending direction, degree, and cycle were changed according to the photoirradiation direction, intensity, and frequency. We not only systematically analyzed the mechanism of these phenomena, but also reproduced the difference in bending behavior through simulation and confirmed that the existence of $Ti_3C_2T_x$ layer plays an important role in determining the photothermally driven bending. Additionally, the ability of $Ti_3C_2T_x$-coated enol-**1** crystal to be actuated by tissue-penetrating NIR light enabled the crystals to bend regardless of whether they are surrounded or entirely covered by agar phantoms with elastic moduli similar to those of biological tissue, and the high cell viability of both $Ti_3C_2T_x$ nanosheets and enol-**1** molecules indicated the potential use of hybrid crystals in biological environments. The method of $Ti_3C_2T_x$ coating to broaden the driving wavelength range of photomechanical molecular crystals has been demonstrated not only in salicylideneaniline (enol-**1** or *p*-COPh-SA) molecular crystals but also in anisole crystals, suggesting the possibility of future expansion and application of this technique to a wider range of molecular crystals.

In addition, this study first proposed a new concept of photomechanical crystals through hybridization of photothermal materials and photomechanical crystals. Photothermal materials have been actively developed as: i) plasmonic noble metals; ii) transition metal-oxides and -chalcogenides;iii) carbon-based nanomaterials; and iv) polymeric materials, but their applications so far have been mainly focused on photothermal therapy.[37–47] Starting with our study, strategies to hybridize photothermal materials and photomechanical crystals and exploit photothermal effect over a wide optical wavelength range are expected to pave the way for the development of innovative light-driven mechanical crystals.

4. Experimental Section

Synthesis of 2D $Ti_3C_2T_x$ MXene Nanosheets: In a Teflon beaker, 1.6 g of lithium fluoride (LiF, 99.9%, Sigma-Aldrich) was dissolved in a mixture of 15 mL of concentrated hydrochloric acid (HCl, 37%) and 5 mL of deionized water. Then, 1.0 g of titanium aluminum carbide powder (Ti_3AlC_2, 40–60 µm micropowder (99.9%), Nanografi) was gradually added under gentle stirring. The etching reaction lasted for 24 h at 35 °C. After 24 h, the acidic mixture was transferred to a 50 mL centrifuge conical tube. The mixture was centrifuged (6000 rpm, 10 min) and washed with deionized water for several times until the pH reached ≈6. The concentration of the $Ti_3C_2T_x$ aqueous solution was concentrated to 50 mg mL^{-1} for coating on the enol-**1** crystals

*Preparation of p-Chlorosalicylideneaniline (Enol-**1**) Crystals*: Enol-**1** was synthesized through the condensation of 3,5-di-*tert*-butylsalicylaldehyde and 4-chroloaniline by microwave heating (Monowave 300; Anton Paar). Single rod-shaped enol-**1** crystals were obtained by slow evaporation of acetone solution (200 mg mL^{-1}) at room temperature under atmospheric pressure. One edge of rod-shaped enol-**1** crystal was fixed to a glass plate. The obtained crystals were treated by oxygen plasma (75 W, 100 sccm, 30 s) using a laboratory plasma cleaner (PIE Scientific) for coating $Ti_3C_2T_x$ solution dispersed in deionized water. The droplets of $Ti_3C_2T_x$ aqueous solution (50 mg mL^{-1}) were loaded on the plasma-treated crystals for entirely coating to the top surface.

Preparation of 2,4-Dinitroanisole (Anisole) Crystals: 2,4-dinitroanisole (TCI Chemicals) was used as-received, without further purification. 300 mg of 2,4-dinitroanisole was dissolved in methanol (4 mL) with heating, and the resultant solution was cooled in a refrigerator at 5 °C for a few tens of minutes to obtain transparent rod-shaped crystals. The $Ti_3C_2T_x$ coating was processed in the same way as enol-**1** crystals.

Preparation of N-3,5-di-tert-Butylsalicylidene-4-Benzoylaniline (p-COPh-SA) Crystals: *p-COPh-SA* was synthesized using a microwave reactor (Monowave 300; Anton Paar), as described in a previous paper by the authors.[15] Single orange rod-shaped crystals of *p-COPh-SA* were obtained by slow evaporation of the solution in methanol. The $Ti_3C_2T_x$ coating was processed in the same way as enol-**1** and anisole crystals.

Observation of Crystal Beam Bending and Temperature Increase: Ultraviolet (UV, 365 nm), visible (455, 660 nm) and near-infrared (NIR, 810 nm) light were irradiated to the top surface of the crystal beam sample by LED light sources (365 nm: M365L4, 455 nm: M455L4, 660 nm: M660L4, 810 nm: M810L4; Thorlab) equipped with a collimator lens (SM2F32-A; thorlab) using an LED driver (DC4104; Thorlab). A USB microscope camera (TOOLCRAFT) was set from the side of the crystal and monitored the crystal bending upon photoirradiation at 30 frames per second (fps). Repetitive bending by the pulsed NIR light was observed by high-speed camera (M205 FA; Leica) at 1000 fps. Pulsed light was generated as square waves (duty ratio: 50%) by the external transistor-transistor logic control of the LED driver (LEDD1B; thorlab) using an Arduino UNO microcomputer device. The bending angle of the crystal was automatically analyzed using Tracker, a video analysis and modeling tool. Surface temperature increase of samples during UV, visible light, and NIR laser irradiation was confirmed using an IR thermal imaging camera (ETS3; FLIR) at 9 fps.

Crystal Beam Bending Simulation: Finite element analysis simulations of the photothermally driven bending were performed using COMSOL Multiphysics software.[54] A simplified 2D analysis geometry of the cross-section face of the $Ti_3C_2T_x$-coated crystal was created using SolidWorks software for considering heat conduction. For $Ti_3C_2T_x$, the thermal conductivity and the density were set to 2.84 W m^{-1} K^{-1}[55] and 4 g cm^{-3},[56] respectively, and the specific heat capacity was altered to the similar value of the similar materials (SiC), 0.607 J g^{-1} K^{-1}.[57] For enol-**1** crystal, the density was set to 1.156 g cm^{-3},[13] and the heat conductivity and the specific heat capacity were altered to the values of the similar salicylideneaniline crystals: 0.15 W m^{-1} K^{-1} and 1.65 J g^{-1} K^{-1}, respectively.[16] The 2D geometry of the cross-section surface of the crystal was divided into elements via the meshing process, and some initial conditions were applied to the specific elements. The non-steady heat conduction was simulated by using COMSOL finite element solver.[54] Bending angles were estimated according to the previous report.[16] Detailed procedures of the non-steady heat conduction are described in Note S2, Supporting Information.

Preparation of Agar Phantoms and Insertion of Crystals into Phantoms: To prepare an aqueous agar solution, 0.7 g of agar ($C_{12}H_{18}O_9$) powder (ultrapure, Alfa Aesar) was mixed with 100 mL of deionized water and heated using a microwave oven. The agar wall was made by pouring the clear agar solution into the mold and cooling it. To cover the $Ti_3C_2T_x$/enol-**1** crystal with an agar phantom, two slide glasses were attached to the top and bottom of the crystal sample at a distance of 5 mm, and then an agar solution was poured between them and cooled to solidify the agar. To monitor crystal bending, an agar phantom positioned to the left of the crystal was cut using a razor blade.

Cell Culturing: The human skin fibroblast cells, BJ (American Type Culture Collection), were cultured with high-glucose Dulbecco's modified

© 2023 The Authors. Advanced Functional Materials published by Wiley-VCH GmbH

16163028, 2023, 47, Downloaded from https://onlinelibrary.wiley.com/doi/10.1002/adfm.202305916 by Koc University, Wiley Online Library on [05/02/2024]. See the Terms and Conditions (https://onlinelibrary.wiley.com/terms-and-conditions) on Wiley Online Library for rules of use; OA articles are governed by the applicable Creative Commons License

Eagle's medium (DMEM, Gibco) supplemented with 10% fetal bovine serum (Gibco) and 1% penicillin/streptomycin (Gibco) in a 75-cm^2 polystyrene cell culture flasks at 37 °C and 5% CO_2. Cells were detached from the surface using trypsin (0.25 wt%)/EDTA solution (Gibco) at 80% confluency.

*Cell Viability Test of $Ti_3C_2T_x$ Nanosheets and Enol-**1***: For the biocompatibility test, the cells from human skin fibroblasts (BJ, ATCC) were seeded in a 96-well plate with a black/clear bottom (Corning) at a concentration of 1×10^4 cells $well^{-1}$ the day before the experiment to allow the cells to attach to the bottom of the plate. The following day, the media of BJ cells were changed with $Ti_3C_2T_x$ nanosheets and enol-**1** containing solutions prepared at different concentrations (10, 20, 50, 100, and 200 µg mL^{-1} in DMEM). After incubating the cells with $Ti_3C_2T_x$ nanosheets and enol-**1** solutions for 24, 48, and 72 h, the viabilities of BJ fibroblasts were tested at defined time intervals using the CellTiter-Glo assay (Promega), following the previously reported method.[58] The viability of treated fibroblasts based on untreated fibroblasts, for which viability was assumed as 100%. All the experiments were performed in triplicates.

Supporting Information

Supporting Information is available from the Wiley Online Library or from the author.

Acknowledgements

D.W.K. and Y.H. contributed equally to this work. This research was financially supported by National Research Foundation of Korea (NRF-2022R1A6A3A03063349) for D.W.K, JSPS Grant-in-Aid for Scientific Research B (17H03107) for H.K., JSPS Research Fellowship for Young Scientists (21J20125) for Y.H., JSPS Overseas Challenge Program for Young Researchers for Y.H., and the Grant-in-Aid for Young Scientists (Early Bird) at Waseda Research Institute for Science and Engineering for Y.H. Y.H. and S.H. thank the Graduate Program for Power Energy Professionals in Waseda University. Y.H. thanks to Mayuka Iida for her help in experiments. This work was funded by the Max Planck Society.

Open access funding enabled and organized by Projekt DEAL.

Conflict of Interest

The authors declare no conflict of interest.

Data Availability Statement

The data that support the findings of this study are available from the corresponding author upon reasonable request.

Keywords

actuators, broad-wavelength, molecular crystals, MXene, photothermal effect

Received: May 26, 2023
Revised: June 29, 2023
Published online: July 12, 2023

[1] W. M. Awad, D. W. Davies, D. Kitagawa, J. M. Halabi, M. B. Al-Handawi, I. Tahir, F. Tong, G. Campillo-Alvarado, A. G. Shtukenberg, T. Alkhidir, Y. Hagiwara, M. Almehairbi, L. Lan, S. Hasebe, D. P. Karothu, S. Mohamed, H. Koshima, S. Kobatake, Y. Diao, R. Chandrasekar, H. Zhang, C. C. Sun, C. Bardeen, R. O. Al-Kaysi, B. Kahr, P. Naumov, *Chem. Soc. Rev.* **2023**, *52*, 3098.
[2] E. Ahmed, D. P. Karothu, M. Warren, P. Naumov, *Nat. Commun.* **2019**, *10*, 3723.
[3] T. Kim, H. Choi, H. Choi, J. S. Kim, D. H. Kim, U. Jeong, *Electrochim. Acta* **2022**, *415*, 140259.
[4] G. Stoychev, A. Kirillova, L. Ionov, *Adv. Opt. Mater.* **2019**, *7*, 1900067.
[5] K. Hou, D. Guan, H. Li, Y. Sun, Y. Long, K. Song, *Sci. Adv.* **2021**, *7*, eabh3051.
[6] I. K. Han, T. Chung, J. Han, Y. S. Kim, *Nano Convergence* **2019**, *6*, 18.
[7] M. Li, X. Wang, B. Dong, M. Sitti, *Nat. Commun.* **2020**, *11*, 3988.
[8] H. Koshima, *Mechanically Responsive Materials for Soft Robotics*, Wiley-VCH, Weinheim, Germany **2019**.
[9] M. Zhang, H. Shahsavan, Y. Guo, A. Pena-Francesch, Y. Zhang, M. Sitti, *Adv. Mater.* **2021**, *33*, 2008605.
[10] M. R. A. Bhatti, A. Kernin, M. Tausif, H. Zhang, D. Papageorgiou, E. Bilotti, T. Peijs, C. W. M. Bastiaansen, *Adv. Opt. Mater.* **2022**, *10*, 2102186.
[11] H. Koshima, S. Hasebe, Y. Hagiwara, T. Asahi, *Isr. J. Chem.* **2021**, *61*, 683.
[12] P. Naumov, D. P. Karothu, E. Ahmed, L. Catalano, P. Commins, J. M. Halabi, M. B. Al-Handawi, L. Li, *J. Am. Chem. Soc.* **2020**, *142*, 13256.
[13] S. Hasebe, Y. Hagiwara, K. Hirata, T. Asahi, H. Koshima, *Mater. Adv.* **2022**, *3*, 7098.
[14] S. Hasebe, Y. Hagiwara, K. Takechi, T. Katayama, A. Furube, T. Asahi, H. Koshima, *Chem. Mater.* **2022**, *34*, 1315.
[15] Y. Hagiwara, T. Taniguchi, T. Asahi, H. Koshima, *J. Mater. Chem. C* **2020**, *8*, 4876.
[16] S. Hasebe, Y. Hagiwara, J. Komiya, M. Ryu, H. Fujisawa, J. Morikawa, T. Katayama, D. Yamanaka, A. Furube, H. Sato, T. Asahi, H. Koshima, *J. Am. Chem. Soc.* **2021**, *143*, 8866.
[17] H. Koshima, K. Takechi, H. Uchimoto, M. Shiro, D. Hashizume, *Chem. Commun.* **2011**, *47*, 11423.
[18] H. Koshima, H. Nakaya, H. Uchimoto, N. Ojima, *Chem. Lett.* **2012**, *41*, 107.
[19] R. O. Al-Kaysi, C. J. Bardeen, *Adv. Mater.* **2007**, *19*, 1276.
[20] H. Koshima, N. Ojima, H. Uchimoto, *J. Am. Chem. Soc.* **2009**, *131*, 6890.
[21] S. Kobatake, S. Takami, H. Muto, T. Ishimawa, M. Irie, *Nature* **2007**, *446*, 778.
[22] T. Taniguchi, A. Kubota, T. Moritoki, T. Asahi, H. Koshima, *RSC Adv.* **2018**, *8*, 34314.
[23] P. Naumov, S. C. Sahoo, B. A. Zakharov, E. V. Boldyreva, *Angew. Chem., Int. Ed.* **2013**, *125*, 10174.
[24] D. Kitagawa, H. Nishi, S. Kobatake, *Angew. Chem., Int. Ed.* **2013**, *125*, 9490.
[25] T. Taniguchi, H. Sato, Y. Hagiwara, T. Asahi, H. Koshima, *Commun. Chem.* **2019**, *2*, 19.
[26] G. Hong, A. L. Antaris, H. Dai, *Nat. Biomed. Eng.* **2017**, *1*, 0010.
[27] Y. Cai, Z. Wei, C. Song, C. Tang, W. Han, X. Dong, *Chem. Soc. Rev.* **2019**, *48*, 22.
[28] M. Sitti, D. S. Wiersma, *Adv. Mater.* **2020**, *32*, 1906766.
[29] M. Sitti, *Mobile Microrobotics*, The MIT Press, Cambridge, MA, USA **2017**.
[30] A. I. Bunea, D. Martella, S. Nocentini, C. Parmeggiani, R. Taboryski, D. S. Wiersma, *Adv. Intell. Syst.* **2021**, *3*, 2000256.
[31] S. Tadepalli, J. M. Slocik, M. K. Gupta, R. R. Naik, S. Singamaneni, *Chem. Rev.* **2017**, *117*, 12705.
[32] M. Naguib, M. W. Borsoum, Y. Gogotsi, *Adv. Mater.* **2021**, *33*, 2103393.
[33] M. Alhabeb, K. Maleski, B. Anasori, P. Lelyukh, L. Clark, S. Sin, Y. Gogotsi, *Chem. Mater.* **2017**, *29*, 7633.
[34] H. Lin, X. Wang, L. Yu, Y. Chen, J. Shi, *Nano Lett.* **2017**, *17*, 384.
[35] R. Li, L. Zhang, L. Shi, P. Wang, *ACS Nano* **2017**, *11*, 3752.
[36] D. Xu, Z. Li, L. Li, J. Wang, *Adv. Funct. Mater.* **2020**, *30*, 2000712.
[37] H. Lin, Y. Chen, J. Shi, *Adv. Sci.* **2018**, *5*, 1800518.

© 2023 The Authors. Advanced Functional Materials published by Wiley-VCH GmbH

16163028, 2023, 47, Downloaded from https://onlinelibrary.wiley.com/doi/10.1002/adfm.202305916 by Koc University, Wiley Online Library on [05/02/2024]. See the Terms and Conditions (https://onlinelibrary.wiley.com/terms-and-conditions) on Wiley Online Library for rules of use; OA articles are governed by the applicable Creative Commons License

[38] Z. Huang, X. Cui, S. Li, J. Wei, P. Li, Y. Wang, C. S. Lee, *Nanophotonics* **2020**, *9*, 2233.
[39] G. Liu, J. Zou, Q. Tang, X. Yang, Y. Zhang, Q. Zhang, W. Huang, P. Chen, J. Shao, X. Dong, *ACS Appl. Mater. Interfaces* **2017**, *9*, 400077.
[40] Y. Li, L. Ding, Y. Guo, Z. Liang, H. Cui, J. Tian, *ACS Appl. Mater. Interfaces* **2019**, *11*, 41440.
[41] R. Li, X. Ma, J. Li, J. Cao, H. Gao, T. Li, X. Zhang, L. Wang, Q. Zhang, G. Wang, C. Hou, Y. Li, T. Palacios, Y. Lin, H. Wang, X. Ling, *Nat. Commun.* **2021**, *12*, 1587.
[42] J. T. Robinson, S. M. Tabakman, Y. Liang, H. Wang, H. S. Casalongue, D. Vinh, H. Dai, *J. Am. Chem. Soc.* **2011**, *133*, 6825.
[43] J. T. Robinson, K. Welsher, S. M. Tabakman, S. P. Sherlock, H. Wang, R. Luong, H. Dai, *Nano Res.* **2010**, *3*, 779.
[44] L. Cheng, J. Liu, X. Gu, H. Gong, X. Shi, T. Liu, C. Wang, X. Wang, G. Liu, H. Xing, W. Bu, B. Sun, Z. Liu, *Adv. Mater.* **2014**, *26*, 1886.
[45] X. Qian, S. Shen, T. Liu, L. Cheng, Z. Liu, *Nanoscale* **2015**, *7*, 6380.
[46] S. S. Chou, B. Kaehr, J. Kim, B. M. Foley, M. De, P. E. Hopkins, J. Huang, C. J. Brinker, V. P. Dravid, *Angew. Chem., Int. Ed.* **2013**, *52*, 4160.
[47] Z. Xiao, C. Xu, X. Jiang, W. Zhang, Y. Peng, R. Zou, X. Huang, Q. Liu, Z. Qin, J. Hu, *Nano Res.* **2016**, *9*, 1934.
[48] K. Ishizaki, R. Sugimoto, Y. Hagiwara, H. Koshima, T. Taniguchi, T. Asahi, *CrystEngComm* **2021**, *23*, 5839.
[49] M. N. Iizuka, M. D. Sherar, I. A. Vitkin, *Lasers Surg Med* **1999**, *25*, 159.
[50] A. M. Handorf, Y. X. Zhou, M. A. Halanski, W. J. Li, *Organogenesis* **2015**, *11*, 1019687.
[51] N. O. Dogan, H. Ceylan, E. Suadiye, D. Sheehan, A. Aydin, I. C. Yasa, A.-M. Wild, G. Richter, M. Sitti, *Small* **2022**, *18*, 2204016.
[52] V. Sridhar, E. Yildiz, A. Rodríguez-Camargo, X. Lyu, L. Yao, P. Wrede, A. Aghakhani, B. M. Akolpoglu, F. Podjaski, B. V. Lotsch, M. Sitti, *Adv. Mater.* **2023**, *35*, 2301126.
[53] Y. Hagiwara, S. Hasebe, H. Fujisawa, J. Morikawa, T. Asahi, H. Koshima, *Nat. Commun.* **2023**, *14*, 1354.
[54] COMSOL Multiphysics v. 5.6 COMSOL AB, Stockholm, Sweden, 2020, [online] Available: www.comsol.com.
[55] L. Chen, X. Shi, N. Yu, X. Zhang, X. Du, J. Lin, *Materials* **2018**, *11*, 1701.
[56] M. R. Lukatskaya, S. Kota, Z. Lin, M. Q. Zhao, N. Shpigel, M. D. Levi, J. Halim, P. L. Teberna, M. W. Barsoum, P. Simon, Y. Gogotsi, *Nat. Energy* **2017**, *2*, 17105.
[57] G. V. Samsonov, *Refractory Carbides*, Springer, New York **1974**.
[58] N. O. Dogan, U. Bozuyuk, P. Erkoc, A. C. Karacakol, A. Cingoz, F. Seker-Polat, M. A. Nazeer, M. Sitti, T. Bagci-Onder, S. Kizilel, *Adv. Nanobiomed. Res.* **2022**, *2*, 2100033.

© 2023 The Authors. Advanced Functional Materials published by Wiley-VCH GmbH

16163028, 2023, 47, Downloaded from https://onlinelibrary.wiley.com/doi/10.1002/adfm.202305916 by Koc University, Wiley Online Library on [05/02/2024]. See the Terms and Conditions (https://onlinelibrary.wiley.com/terms-and-conditions) on Wiley Online Library for rules of use; OA articles are governed by the applicable Creative Commons License